DISTINCT TEMPORAL PATTERNS OF NUCLEAR AND NUCLEOLAR REMODELING PRECEDING CELL DEATH INDUCED BY CHEMICAL AND PHYSICAL STRESSORS

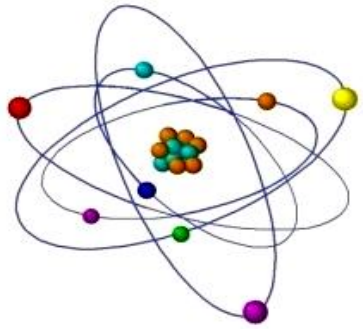

[1]Anastasia Datunashvili, [2,3]Lili Nadaraia,
[2]Natia Makhatadze, [1]Lia. Taziashvili, [4]Mikheil Nanikashvili,
[5]Levan Rusishvili, [2]Pavle Tchelidze*

[1]New Vision University, Georgia;
[2]Carl Zeiss Scientific and Education Center, Georgia;
[3]Republic Center of Structure Research, Georgian Technical University, Georgia;
4Georgian Scientific Industries, Georgia,
5Iv. Javakhishvili Tbilisi State University, Georgia

DOI: 10.63465/rrs6202611765 Corresponding author: pavel.tchelidze@univ-reims.fr

ABSTRACT: *Two major classes of prominently apoptogenic stressors—physical and chemical—were employed to resolve the detailed chronology of chromatin and nucleolar pre-mortal remodeling in HeLa cells stably expressing histone H2B–GFP. Physical damage was induced by ionizing γ-irradiation and non-ionizing heat shock, whereas chemical stress was triggered by the rDNA-intercalating anticancer agents actinomycin D and cisplatin. Actinomycin D served as a classical model of rRNA synthesis inhibition, reliably inducing canonical nucleolar segregation, and was used as a reference standard to compare the chronology and dynamics of nuclear and nucleolar deformations elicited by other stressors. Cisplatin was applied to evaluate whether chemically induced DNA damage produces nucleolar responses comparable to those triggered by physical factors.*

Long-term live-cell 2D time-lapse imaging was performed to monitor GFP-tagged nucleosomal chromatin behavior, with particular emphasis on intra- and perinucleolar chromatin dynamics. To assess nucleolar remodeling, stress-induced three-dimensional redistribution of the RNA polymerase I–associated transcription factor UBTF was analyzed by immunolabeling followed by 3D reconstruction. Ourresults demonstrate stressor-specific patterns of intranucleolar 3D reorganization of UBTF and nucleolus-associated condensed chromatin. These findings provide structural insights relevant to chemo- and radiotherapy outcomes and may inform strategies aimed at enhancing nucleolar stress, mitotic catastrophe, and apoptosis in resistant malignancies.

Keywords: Irradiation, Mitotic Catastrophe, Nuclear and Nucleolar Stress, Pre-Mortal Remodeling

INTRODUCTION

Molecular events related to ribosomal genes (r-genes) transcription, nascent or pre-ribosomal RNA (pre-rRNA) processing and pre-ribosomal subunits assembling are shared among five nucleolar functional sub-compartments, defined in electron microscopic (EM) studies as nucleolar components (NCs). This five includes: (i) fibrillar centers (FCs), (ii) dense fibrillar component (DFC), (iii) granular component (GC), (iv) the 3D system of nucleolus-associated chromatin (NAC system), comprising peri- and intra-nucleolar condensed chromatin (PCC and ICC respectively) and (v) interstices and large nucleolar vacuoles (NI and NV, respectively). It is firmly established that r-genes transcription occurs inside interface area between FC and the juxtaposed DFC, a territory, known as transcriptionally active r-genes localization site that can be fluorescently detected by light microscope (LM) immunocytochemistry, using RNA Polymerase I (Pol I), upstream binging transcription factor (UBTF) etc. as specific bio-markers. The DFC corresponds to the NC where early processing of nascent pre-rRNA takes place, confirmed by the presence of specific markers, such as fibrillarin, nucleolin etc.

The more advanced steps of pre-rRNA maturation occur on the periphery of the DFC, whereas late processing and pre-ribosome assembling (specific markers: nucleolar proteins B23, NOP52 etc.; different ribosomal proteins) develop within nucleolar territory known as GC. Nucleolus-associated DNA (naDNA) domains, defined as NAC system presumably contains non-ribosomal sequences, while functionally less studied NI and NV may contribute to the spatial arrangement of the ICC. The latter can be readily visualized inside the nucleolus using histone H2B labeling. FCs are interconnected with each other via ICC, thus forming together with PCC unit complex, so that concerted contraction of NAC components put NCs in motion [1-9].

Posed as central biosynthetic hub for ribosome biogenesis, the nucleolus plays a critical role in maintaining homeostasis of whole cellular metabolism. The LM and EM organization of the nucleolus resiliently adapts the 3D topography of NCs in response to various cellular stress conditions, including metabolic changes, differentiation signals, neoplastic transformation etc. [7, 8, 10-17]. Thus, genotoxic impact of a bulk of DNA damaging exogenous factors results in severe metabolic shifts in ribosome production, compulsory leading to mitotic catastrophe (MC), followed by cellular death, expressed through apoptosis, necrosis, autophagy, or mixed forms of post-MC death [18-33].

A number of anti-cancer drugs, acting via inhibition of ribosome biogenesis, produce typical picture of the nucleolar stress, displaying strongly specific spatial displacement of NCs and known as nucleolar segregation or capping [7, 8, 11, 12, 14, 15, 34]. Among these, prominently apoptogenic factor actinomycin D (AMD) has long been considered as the oldest but the most effective model for visualization of nucleolar stress in cells and tissues. Since first experiments, using AMD as rRNA synthesis specific inhibitor, the ability of FCs and DFC to move in crowded nucleolar volume and fuse, thus inducing nucleolar stress linked structural pattern, has firmly been established. In contrast, pre-mortal reaction in response to certain physical factors that severely damage DNA replication/transcription capability, drastically differs from the nucleolar inactivation pattern induced by chemical stressors. To illustrate, such a powerful

apoptogenic impact as ionizing irradiation doesn't produce classical picture of nucleolar segregation [35, 36]. In addition, although the nucleolus is considered as the major cellular stress-sensing site, another physical factor, namely non-ionizing thermic shock [12], has been employed. Noteworthy, the long-term dynamics of nucleolar remodeling after temperature-induced nucleolar stress has not been elucidated so far. On the other hand, a number of prominently apoptogenic anti-cancer molecules, can produce distinct morphological and molecular states of nucleolar stress [7, 8, 11, 14, 15, 17] while nothing is known, whether they induce drug-specific chronology and dynamics of pre-mortal nuclear and nucleolar behavior and nucleolar proteins redistribution.

Hence, the comprehensive 3D/4D insight to cross-specify factor-dependent long-term chronology and dynamics of pre-apoptotic nuclear and nucleolar behavior after action of different physical (e.g. γ–yrradiation and thermal shock) and chemical stressors (e.g. AMD and cisplatin) is obviously of paramount interest.

Present study suggests long-term 2D/4D dynamics and 3D structural remodeling of nucleus and nucleolus provoked by physical and chemical stressors, with special regard to NAC 3D reorganization and mobility. The particular focus on NAC behavior was stipulated by our hypothetical mechanism of intranucleolar inactivation dynamics, involving the mobility of the whole NAC system on the one hand, and its structural integrity with the FC/DFC assembly. We believe that the simultaneous contraction of the ICC and PCC and perinucleolar dislocation of ICC that induce the motion of the UBTF-positive FCs.

Live cell experiments as well as live and fixed cell imaging have been performed using, He-La culture stably tagged by histone H2B-GFP. Following stressors have been applied: (i) to induce chemical stress we resorted to 0.05 and 0.5 μg/ml doses of AMD, while cisplatin (Cis-Pt) has been applied in doses of 250 and 500 μg/ml. Action of both lasted during 24 hours under 2D/4D image acquisition. AMD was used as the most effective inductor of classical morphological pattern of the nucleolar stress and as etalon to analyze the chronology and dynamics of nuclear/nucleolar deformations produced by other factors; (ii) ionizing γ-irradiation applied in doses of 15 and 30 Gy, with following post-irradiation time-lapse imaging over 72 hours; (iii) thermic shock induced by exposure of culture at 42oC during 2 hours [12] followed by post-treatment time-lapse 2D/4D image acquisition over 24 hours. Consistent with our previous approach, stress-induced 3D redistribution of FCs was analyzed using anti-UBTF immunolabeling to resolve alterations in their LM morphology and spatial positioning.

This work represents the initial stage of a broader investigation aimed at elucidating the structural basis of pre-mortal nucleolar stress dynamics. By focusing on morpho-functional remodeling of the nucleolus and its chromatin framework, the present study establishes a structural foundation for subsequent analyses of the underlying molecular mechanisms. Such integration is essential for understanding how nucleolar stress responses influence clinical outcomes, particularly in the context of radiotherapy (RT) and chemotherapy (CT). In this regard, therapeutic strategies designed to MC may improve RT/CT efficacy, especially in apoptosis-resistant malignancies, where alternative cell death pathways become critical determinants of treatment response.

MATERIAL AND METHODS

The methodological approaches employed in this study—including cell culture procedures, radiation setup, live-cell 2D/4D imaging, fixed-cell 3D reconstruction, microscopy instrumentation, and image-processing software—were largely consistent with those described in our previous reports [7, 8, 35, 36]. Below, we provide a brief summary of the principal technical procedures relevant to the present investigation.
Irradiation was conducted with a gamma irradiation device, utilizing ^{137}Cs as the radiation source at a dose rate of 1.1 Gy/min. The irradiation dose was set at 30 Gy per interval.

2.1. Cell Cultivation and Maintenance

As a widely used model for studying cell death-related morphology, we utilized cultured He-La cell stably expressing the histone H2B-GFP fusion protein (courtesy of Prof. O. Piot, University of Reims Champagne-Ardenne, France). This model provides stable nucleoplasmic and intranucleolar fluorescence with minimal photobleaching, enabling long-term (up to 72 h) confocal time-lapse imaging. Correspondingly, we used this culture for live-cell analysis of chromatin and nucleolar remodeling during MC. Cells were maintained in DMEM supplemented with 10% calf serum and 1% penicillin/streptomycin at 37 °C and 5% CO_2, routinely passaged, and confirmed to be mycoplasma-free (monthly tests for mycoplasma detection were conducted). Regular reseeding occurred 2-3 times per week based on the cell monolayer reaching late pre-confluent or early confluent stages. To study nucleolar dynamics during γ-irradiation-induced remodeling, we prepared samples in a way that ensured cultures remained sub-confluent even after 72 hours of post-irradiation incubation and/or post-irradiation acquisition of living cell images [see: 7, 8, 12, 35, 36 for details].

2.2. Cell Seeding

Cells were seeded onto collagen-coated glass-bottom dishes (Ø35 mm, MatTek) at 10,000–15,000 cells/mL, following surface preconditioning according previously described protocol. Gentle dropwise seeding or brief agitation after bulk seeding was used to obtain sparsely distributed cell groups suitable for prolonged live imaging and post-irradiation incubation [see: 7, 8].

2.3. Inhibition of rRNA synthesis by AMD and Cis-Pt

To inhibit rRNA synthesis and induce nucleolar segregation, cells were exposed to AMD and Cis-Pt at defined low and high concentrations. AMD was applied at 0.05 µg/ml and 0.5 µg/ml, while Cis-Pt was used at 250 µg/ml and 500 µg/ml. Drug exposure lasted from 1 to 24 h, allowing assessment of both early and late nucleolar responses. Treatments were carried out directly in Petri dishes mounted in a sealed incubation chamber compatible with the LSM 900 confocal microscope (Carl Zeiss, Germany), enabling uninterrupted live-cell observation. Continuous 2D/4D time-lapse imaging was performed for up to 24 h at 37 °C under a controlled CO_2 atmosphere. Prior to drug administration, cultures were rinsed three times with PBS (5 min

per rinse) to remove residual medium components and then incubated in fresh culture medium containing AMD or Cis-Pt for the duration of imaging [7, 8, 15].

2.4. γ-Irradiation

γ-Irradiation was performed at the E. Andronikashvili Institute of Physics (Tbilisi State University, Georgia) using a GUPOS-3M ^{137}Cs irradiator producing the dose rate 1.1 Gy/min. All experimental procedures involving γ-irradiation exposure of cells were approved by the Ethics Committee of the I. Beritashvili Center for Experimental Biomedicine and were conducted in strict adherence to Georgian National Health and Safety Regulations. Dose selection was based on the results of our recent work. Thus earlier, we compared γ-irradiation doses of 10 and 30 Gy selected with reference to clinically relevant radiotherapy paradigms. Exposure to 30 Gy — exceeding conventional single-fraction stereotactic body radiotherapy schedules — elicited markedly stronger cellular and nuclear remodeling, consistent with extensive MC, indicating that dose escalation substantially amplifies nuclear structural disruption [see: 35, 36].

2.5. Heat-shock treatment

Before imaging, cells were transferred to 42 °C for 2.5 h. Time-lapse observation of nuclear and nucleolar changes during the heat-shock period was performed using a custom digital device consisting of a compact digital microscope (GSI, Georgia) installed inside a thermostat. The system was equipped with a monitor placed outside the thermostat, allowing continuous observation and registration of nuclear and nucleolar dynamics throughout the entire heat-shock treatment.

Immediately after heat shock, cells were briefly rinsed with PBS and transferred to fresh incubation medium. Culture dishes were then placed in a sealed incubation chamber for uninterrupted live-cell imaging of post-thermal nuclear and nucleolar recovery dynamics for 24 h at 37 °C in a humidified CO_2 atmosphere. Fixed-cell samples were processed and imaged in parallel as controls:

(i) cells fixed and imaged immediately after exposure to 42 °C for 2.5 h; (ii) heat-treated cells fixed and imaged after 24 h incubation at 37 °C; (iii) untreated cells fixed and imaged after 24 h incubation at 37 °C.

2.6. Immunofluorescence Labeling

Post-fixation immunolabeling was used to visualize FCs using UBTF as marker. Directly conjugated primary monoclonal antibodies were applied after fixation, permeabilization, and blocking. For visualization of UBTF in red AlexaFluor594 conjugated anti-UBF/F-9 fragment (Santa Cruz Biotechnology, USA) monoclonal antibodies, were used. Samples were imaged directly in culture dishes [see: 35, 36].

2.7. 2D/4D Live-Cell Imaging, 3D Reconstruction and Modeling

Live-cell imaging was performed using a Carl Zeiss LSM 900 confocal microscope equipped with Airyscan 2 and environmental control (37 °C, 5% CO_2). GFP fluorescence was excited using low laser power settings to minimize phototoxicity. Z-stacks spanning entire nuclei were acquired in phase-contrast and fluorescence modes with a 0.3 µm step size. Image acquisition and primary processing were performed using ZEN 3.0 software (Carl Zeiss) [see 34, 35 for details]. 2D/4D time-lapse imaging of cells treated with AMD and Cis-Pt was conducted for 24 h with 5-min intervals. 2D time-lapse imaging of γ-irradiated cells was performed over 72 h at 10-min intervals. Heat-shock-treated cells were 2D/4D imaged for 24 h using 10-min intervals. Confocal Z-stacks were reconstructed, rendered, and subjected to surface and volume visualization using ArivisPro 4.4.0 software (Carl Zeiss) to analyze UBTF- positive nucleolar components and NAC structures, generating corresponding 3D models. To evaluate intranucleolar chromatin condensation (ICC) dynamics during nucleolar segregation, time series were visualized as 2D movies using ZEN 3.0 software. Key stages of ICC movement and coalescence during chemical and physical stress were extracted from full time-lapse datasets and presented in chronological galleries or 2D movies according to previously described procedures [see: 7, 35, 36]

RESULTS

3.1. Nuclear and Nucleolar Morphological Profiles in Control and after AMD/CPT Treatment. Chemical Treatment Chronology

At low magnification, both living and fixed cultures predominantly exhibited mononuclear cells, with frequent mitotic figures and occasional apoptotic cells. Histone H2B–GFP fluorescence intensity correlated with chromatin compaction, with the brightest signals corresponding to chromocenters and the PCC ring. Nuclei were typically round or ovoid with mildly irregular contours. Nucleoli appeared as large, dark spherical or elongated territories containing less intensely labeled GFP-positive ICC inclusions [see: 35, 36]. At higher magnification, ICC was consistently observed as clumps or anastomosing cords extending from the PCC ring into the nucleolar interior. 3D reconstructions revealed that PCC forms a continuous, sometimes locally disrupted shell surrounding the nucleolus, from which ICC cords emanate [7]. This organization supports a unified, network-like ICC architecture continuous with the PCC, consistent with earlier LM and ultrastructural observations. 3D analysis of UBTF-positive NCs in control cells demonstrated their tight spatial coupling with the ICC–PCC framework. These UBTF-positive foci were of ~0.3–0.5 µm in mean diameter, being consistently embedded within the ICC network and densely grouped in characteristic “folded necklace” patterns, consistent with FC organization at LM level [see: 7, 8].

Results obtained at different time-points after treatment with AMD and Cis-Pt were analyzed using either randomly selected and/or serial images (Fig. 1, 2) or via movies arranged in form of individual images extracted from whole datasets to show chronologically major morphological changes. Fixed-cell and anti-UBTF labeled samples analyses and corresponding 3D models clearly demonstrate that both inhibitors induced reorganization of UBTF- positive

FCs into crescent-shaped caps positioned at the PCC–nucleolar interface (Fig. 2), a hallmark of chemical nucleolar stress that precedes overt apoptotic degeneration and death [see: 7, 8].

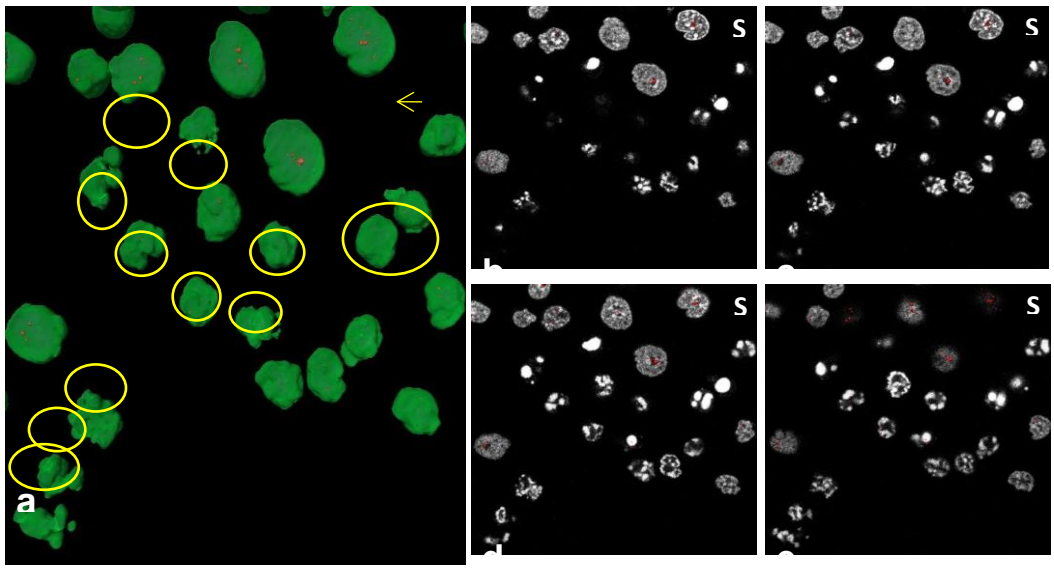

Fig. 1. Massive apoptosis induced by treatment with AMD (0.5 µg/ml) during 8 h. Nuclei of fixed cells after anti-UBTF labeling. a - 3D reconstruction with transparent surface rendering of nuclei (green); interphase FCs were shown in solid red. Note presence of pre-apoptotic cells (marked by yellow arrows) that still exhibiting UBTF-positive FCs. Multiple apoptotic cells were taken in yellow circles. b-e - The same field visualized using non-consecutive serial sections and merged orthogonal slices of nuclei (grayscale) with solid rendering of prominently visible FCs.

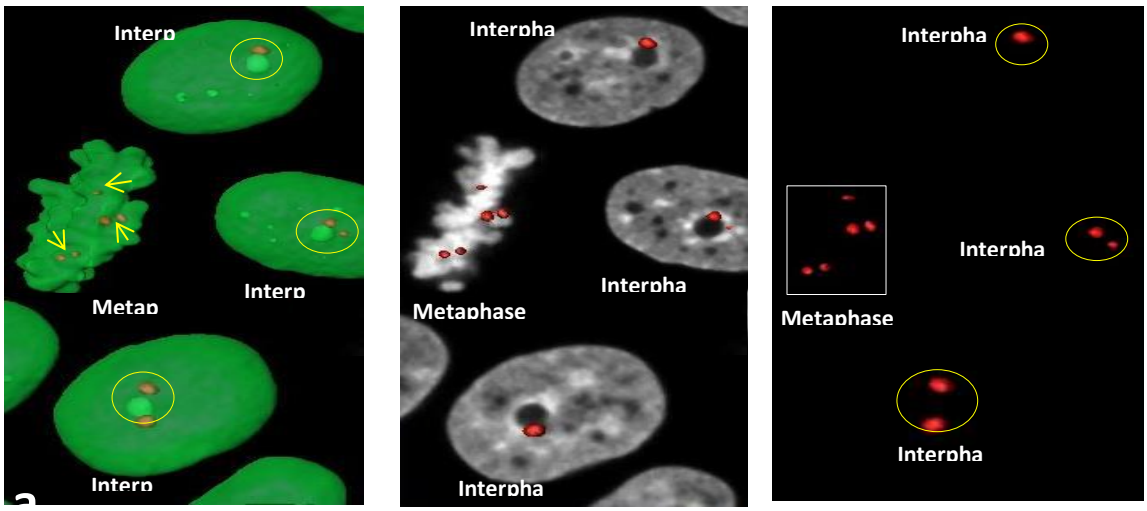

Fig. 2. Nucleolar segregation and capping as a consequence of treatment with Cis-Pt (500 µl) during 8 h as revealed using post-fixation anti-UBTF immunolabeling. Note that mitotic cells still exist. a - 3D reconstruction with transparent surface rendering of nuclei (green); interphase FCs and mitotic NORs (marked by yellow arrows) were shown in solid red. Segregated nucleoli were taken in yellow circles. b - The same field visualized using merged orthogonal slices of nuclei (grayscale) with solid rendering of FCs and NORs (red). Nucleolar caps are clearly seen. c – The same field visualizing 3D reconstruction only. Mitotic NORs were taken in white rectangle, while segregated nucleolar territories with caps were outlined by yellow circles.

In contrast to the structural similarities, the temporal effects of AMD and Cis-Pt were clearly distinct. AMD treatment induced relatively rapid and extensive apoptotic cell death, becoming evident within ~8 h, whereas Cis-Pt–induced massive cell death was markedly delayed, reaching maximal levels at approximately 17 h [see: 7, 12]. Consistently, AMD triggered nucleolar segregation within 3 h, while Cis-Pt–induced nucleolar cap formation occurred later, around the 8 h time point. However, despite these kinetic differences, the morphological sequence of apoptosis triggered by both inhibitors was indistinguishable and consistent with previously described stage-wise apoptotic dynamics [see: 12].

3.2. Distinct Nuclear and Nucleolar Post-Irradiation Morphological Profiles and Post-Irradiation Chronology

The detailed step-wise live-cell chronology of post-irradiation recovery over 72 h, together with accompanying nucleolar structural modifications, has been described previously [see: 35, 36]. Obviously, time-lapse imaging was employed to characterize pre-mortal nuclear and nucleolar morphological changes induced by 30 Gy γ-irradiation. This approach enabled visualization of progressive nuclear and nucleolar damage over 72 h of post-irradiation image acquisition. Importantly, across independent experiments, nuclear and nucleolar alterations consistently followed similar trajectories, becoming prominent after 24–48 h and reaching maximal intensity at 72 h. Following dynamics of developing structural responses we observed: (1) during the initial 12 h post-irradiation, nuclear and nucleolar morphology largely resembled control cells. Nuclei remained ovoid, predominantly with smooth contours, nucleoli were large and irregular, while ICC formed an extensively branched network. In global view, UBTF distributions was indistinguishable from control, indicating preserved FC-ICC organization; (2) between 12 and 24 h, gradual ICC coarsening and thickening of the PCC shell became evident. UBTF-positive strucvtures increased in size but remaining intranucleolar localization and integration within NAC; (iii) within 24 and 48 h post-irradiation period, nuclear deformation intensified. Multinuclear and apoptotic cells became frequent, although occasional mitotic cells persisted. ICC reorganized into large clumps, sometimes forming ring-like structures, accompanied by pronounced and PCC thickening around whole nucleolar surface. UBTF-positive structures enlarged progressively, with sharply defined spherical entities reaching up to ~1 μm – 1.5 μm in mean diameter in some cells, while remaining structurally integrated within the ICC–PCC framework.

Because the most profound nuclear and nucleolar remodeling occurred between 48 and 72 h the present study we focus specifically on the major irradiation-induced nucleolar structural alterations observed at the 72 h post-irradiation time point. At this time massive multinucleation and apoptosis predominated, following a reproducible MC sequence: nuclear invagination, asymmetric fragmentation into micronuclei, and endomitotic division, followed by apoptotic degradation. Accordingly, representative images acquired at the defined 72 h post-irradiation time point capture these principal stage of nuclear and nucleolar remodeling, characterized by extensive mitotic catastrophe (MC), multinucleation, and a marked enlargement of UBTF-positive structures to giant spheroidal forms (Fig. 3). Similarly, to previously reported results by following irradiation-induced temporal changes, many initially ovoid nuclei in surviving cells gradually became irregular, underwent lobulation, and ultimately fragmented through amitotic cleavage and endomitotic division, resulting in multinuclear cells. Throughout all stages γ-irradiation induced progressive compaction and reorganization of NAC without triggering canonical nucleolar segregation. Enlarged UBTF-positive structures persistent ICC–PCC continuity, defining a non-

classical, pre-segregated nucleolar state distinct from that induced by chemical rRNA synthesis inhibitors. Very notably, PCC became evenly thickened around whole nucleolar perimeter/surface [see: 35, 36].

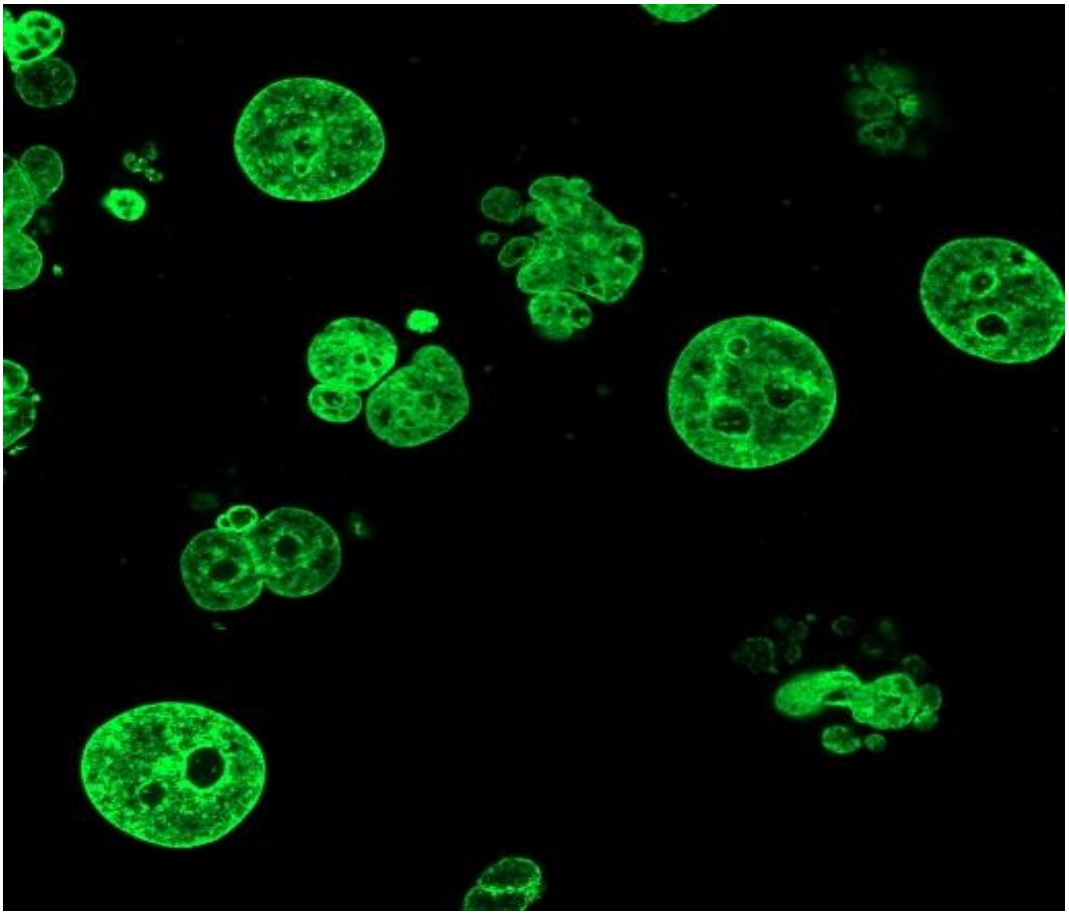

Fig. 3. Structural features of histone H2B-GFP tagged He-La cells exposed to 30 Gy γ-irradiation followed by 72 h of post-irradiation live-cell image acquisition period. These images were taken at low magnification, using fluorescent regime only. Abundancy of post-mitotic catastrophe multinuclear cell population (outlined by yellow circles) exposing signs of asynchronous apoptosis (yellow asterisks) were obvious. A subset of survived cells retaining mononuclear morphology with smooth nuclear outlines (outlined by red circles) were also detected. Even at low magnification prominent ring of PCC and ICC clumps were clearly seen. MC – mitotic catastrophe.

3.3. Distinct Nuclear and Nucleolar Remodeling during Post-Heat-Shock Recovery

A review of the literature revealed a lack of detailed analyses addressing nuclear and nucleolar remodeling during heat-shock treatment and subsequent recovery. To address this gap, 2D/4D time-lapse imaging was performed to monitor heat-shock–induced nuclear and nucleolar structural changes (42 °C for 2.5 h), with particular emphasis on NAC remodeling dynamics. In parallel, 3D reconstructions of fixed cells immunolabeled for UBTF were generated to assess heat-shock–induced spatial reorganization of FCs. Together, these approaches revealed nuclear and nucleolar damage patterns developing during heat-shock and over 24 h of post-treatment recovery that were clearly distinct from those induced by chemical stressors or γ-irradiation. Images acquired at

defined time points covering 0–24 h of post–heat-shock recovery were extracted from full live-cell 2D datasets and are presented in Figure 4.

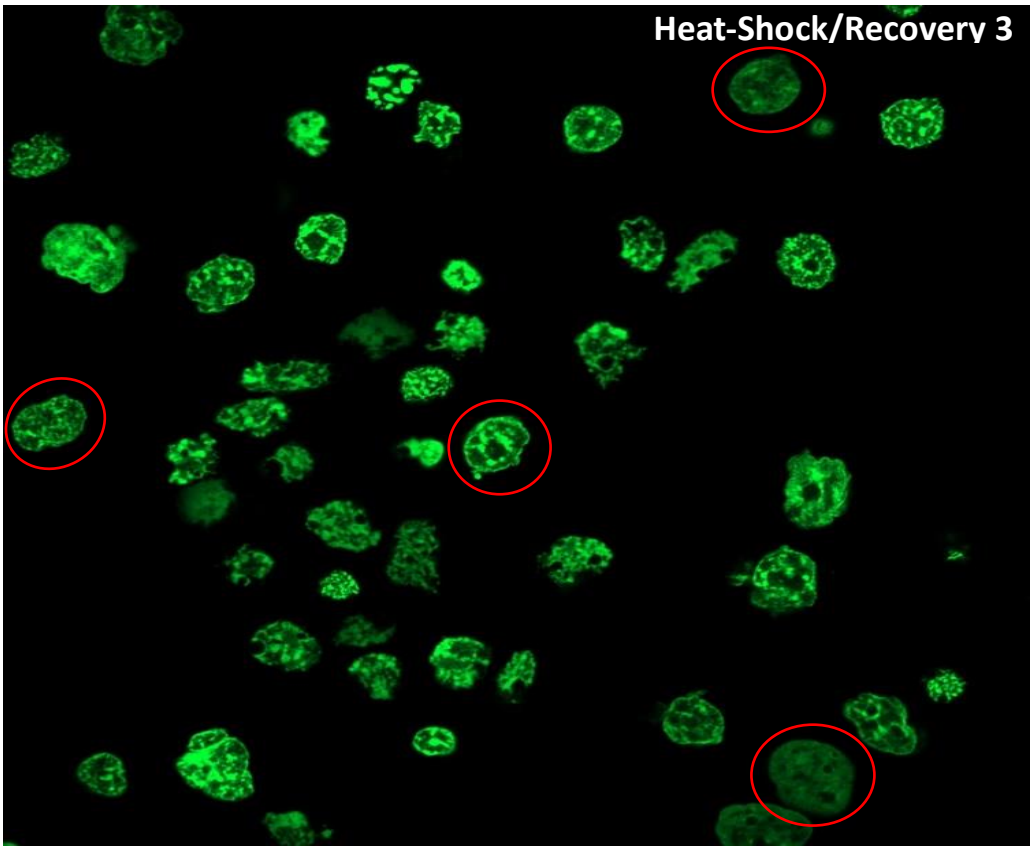

Fig. 4. Heat-shock (2.5 h), post-treatment recovery; time point extracted from whole data set of live-cell imaging at low magnification. The field shows extensive apoptotic degradation, confirming the strong apoptogenic effect of heat-shock. Severely deformed nuclei of pre-apoptotic and apoptotic cells were abundant. Occasional surviving mononuclear cells (red circles) display relatively smooth nuclear contours. Note the pronounced clumping of the PCC ring in the centrally positioned nucleus.

Selected frames from live-cell 4D datasets were further subjected to 3D reconstruction and assembled into galleries to illustrate the principal stages of structural remodeling (Fig. 5). Live-cell imaging and 3D modeling showed that shortly after post-heat-shock recovery onset (0 h – 4 h), many nuclei looked like adopted drastically irregular shapes. In parallel intense micronucleation and apoptotic degradation that reached maximum at 3 h post-treatment recovery time point was registered (Fig, 4). During 8 h recovery nuclear contours further folded, while number of apoptotic cells was quite high and process of micronucleation remained intense. Meanwhile, at prolonged post-heat-shock recovery time points (8 h – 24 h) nuclear contours became gradually smoothened however micronucleation process continued (Fig. 5).

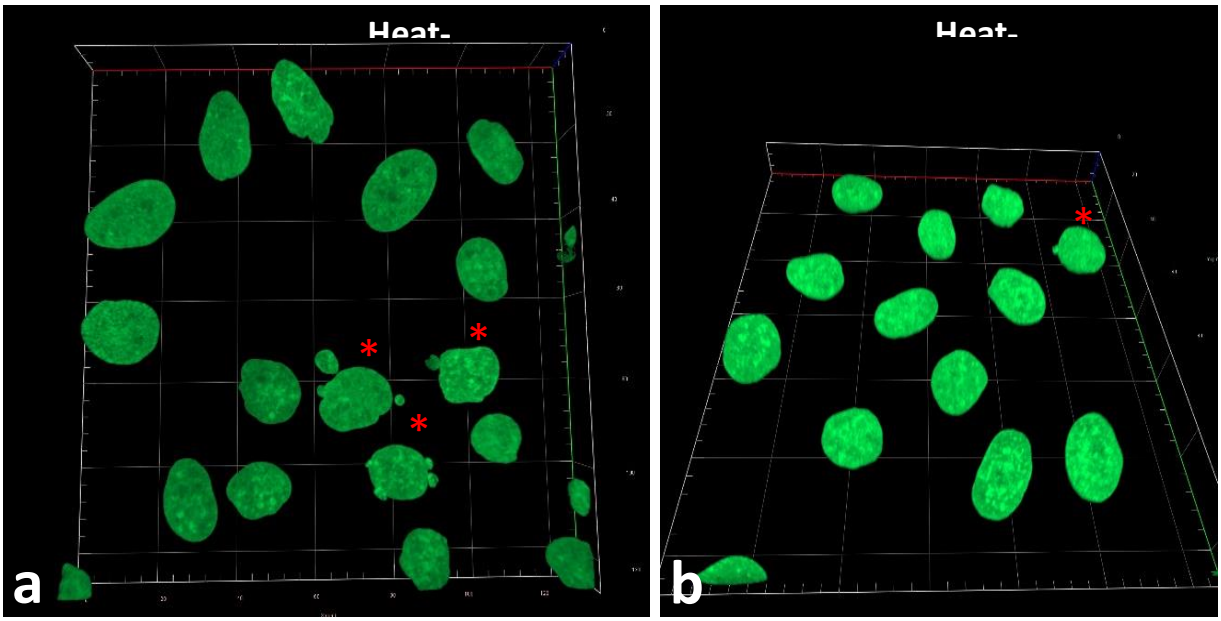

Fig. 5. Heat-shock, 24 h post-treatment recovery; live-cell imaging and 3D reconstruction at low magnification. Although overall nuclear morphology and chromatin organization were largely re-established and resemble control patterns process of micronucleation still continues. a - Three nuclei (red asterisks) generated multiple micronuclei, while resting population largely looks like nuclei of control samples. b - A different field of same preparation showing nucleus (red asterisk) producing only one micronucleus.

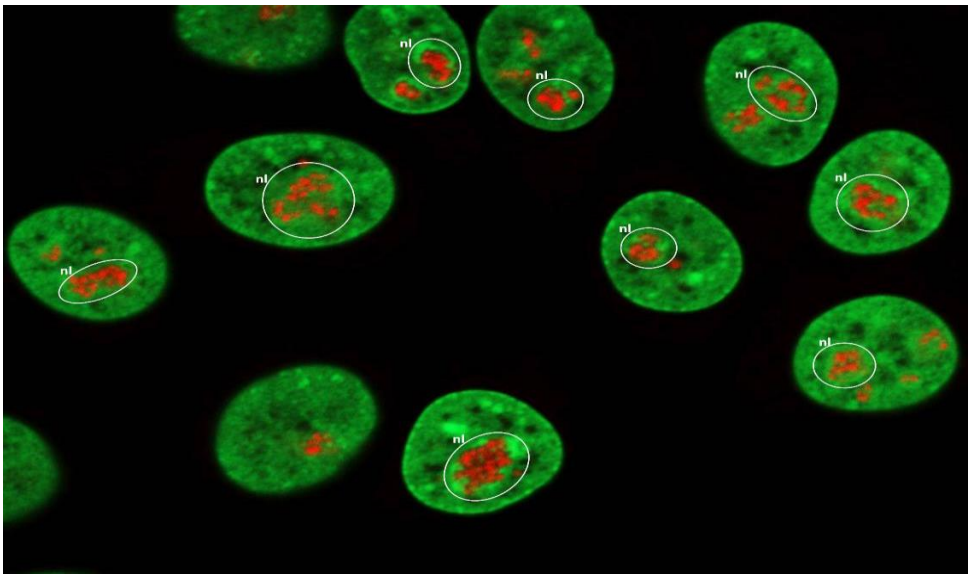

Fig. 6. Heat-shock (42°C, 2.5 h), 24 h post-treatment recovery. Merged histone H2B–GFP (green) and anti-UBTF (red) labeling; nucleolar territories are outlined by white circles. Nuclear morphology and chromatin organization are largely re-established in the majority of cells. UBTF-positive structures regain a grouped intranucleolar arrangement consistent with

Across independent experiments, nucleolar alterations followed were similar and became more pronounced at later recovery stages. Apoptotic degeneration developed asynchronously, while lobulated, and occasionally fragmented via amitotic mechanisms cases were also detected. Occasional MC was detected even at latest (24 h) stages, while by the end of recovery, many surviving cells exhibited nearly completely restored smooth nuclear contours.

Heat-shock responses were predominantly confined to the NAC–FC structural unity, with the PCC shell exhibiting localized disruption characterized by asymmetric coarsening and prominent chromatin clumping. Noteworthy, numerous enlarged up to ~ 0.6-0.9 μm of mean diameter, UBTF-positive structures retained intranucleolar localization and remained integrated within the ICC–PCC framework. Most importantly, these structures did not transform into giant spheroids or crescent-shaped caps, presumably indicating preservation of FC–NAC continuity Concurrently, the ICC network exhibited evident distortion, manifested by its conversion into coarse, intensely GFP-positive chromatin aggregates. In contrast to post–γ-irradiation remodeling, the spatial distribution of UBTF-positive domains after heat shock showed no terminal peripheral translocation of enlarged spheroids or formation of tightly associated PCC–UBTF complexes. Instead, UBTF-positive structures remained dispersed throughout the nucleolar volume, losing their tight grouped organization and becoming more spatially separated. Notably, by the end of the recovery period (24 h), UBTF-positive structures completely restored their clustered intranucleolar organization (Fig. 6).

Importantly, throughout all examined stages, heat-shock induced progressive reorganization of the NAC–UBTF system without triggering canonical nucleolar segregation. Collectively, these morphological features define a non-classical, pre-segregated nucleolar state distinct from both chemically induced rRNA transcriptional inhibition and severe DNA damage caused by γ-irradiation. Heat shock therefore represents a structurally distinct physical stressor producing stress-specific nucleolar remodeling patterns.

DISCUSSION

During last 50 years it became increasingly evident that nucleolar LM and EM, morphological profiles are not a passive structural characteristic but an active reflection of ribosomal biogenesis, transcriptional activity of RNA polymerase I, NAC organization, and cellular stress responses. Changes in nucleolar shape, size, number, and internal architecture—the relative arrangement of ultrastructural functional subcompartments such as FCs, DFC, and GC—have emerged as sensitive indicators of r-genes transcriptional activity, pre-rRNA processing and pre-ribosomal subunits assembling. These nucleolar characteristics manifest across distinct imaging modalities: LM allows the evaluation of nucleolar number, shape, size, whereas EM reveals fine ultrastructural details, including changes in sizes, number and distribution of FCs, their hypertrophy, expansion or disruption of DFC caused by DRB treatment, segregation of NCs accompanied with formation of nucleolar caps emerging during r-genes transcriptional inhibition etc. [7, 8, 12, 14, 17, 34]. During the following decades (including last 10), unremitting attention to nucleolus posing as reliable functional criterion was confirmed by a

bulk of studies [13-17].

In this study, we performed a comparative analysis of nuclear and nucleolar remodeling induced by AMD and Cis-Pt, high-dose γ-irradiation, and heat shock, with particular emphasis on NAC dynamics and the spatial behavior of FC-NAC assemblies. By combining long-term live-cell 2D/4D imaging with 3D structural analysis of immunolabeled fixed cells, we were able to resolve stress-specific morphological trajectories leading to MC, apoptosis, or recovery. Our long-term live-cell observation clearly demonstrated that impact of physical and chemical nucleolar stress factors studied, obligatory leads to apoptotic degradation finalized with cell death.

4.1. Chemical Stress Induces Canonical Nucleolar Segregation with Stress-Specific Kinetics

Chemical inhibition of rRNA synthesis by AMD and Cis-Pt produced classical morphological pattern of nucleolar stress responses. In both cases, UBTF-positive structures (in fact FCs) reorganized into crescent-shaped caps positioned at the interface between PCC and the nucleolar surface. This segregation pattern, previously described as a hallmark of transcriptional arrest–induced nucleolar stress, preceded apoptotic degeneration and cell death.

Importantly, although the structural outcome was similar for both inhibitors, their temporal dynamics differed substantially. Whereas AMD induced rapid nucleolar segregation, followed by massive apoptotic cell death approximately 5 h later, Cis-Pt triggered nucleolar segregation less efficiently. In the latter case, apoptotic degradation was delayed until ~8 h and progressed more gradually. Consequently, extensive apoptotic cell death occurred only around 15-17 h, i.e., approximately 7-9 h later than in AMD-treated cells, highlighting markedly slower nucleolar stress kinetics in response to Cis-Pt compared with AMD.

Despite these kinetic differences, the morphological sequence of apoptotic changes was indistinguishable and fully consistent with previously reported stage-wise apoptotic dynamics [12]. These findings reinforce the concept that chemical rRNA synthesis inhibitors converge on a common nucleolar segregation pathway, while the timing of downstream cell death reflects stressor-specific mechanisms.

4.2. γ-Irradiation Induces Non-Classical Nucleolar Remodeling without Cap Formation

In contrast to chemical stress, high-dose γ-irradiation elicited a fundamentally different nuclear and nucleolar response. Time-lapse imaging over 72 h revealed a reproducible sequence of nuclear deformation, lobulation, and fragmentation, culminating in multinucleation through amitotic cleavage and endomitotic division—hallmarks of MC. These changes became prominent after 24–48 h [35, 36] and were consistently observed across independent experiments.

Strikingly, despite progressive NAC compaction and extensive nuclear damage, γ-irradiation never induced canonical nucleolar segregation accomplished with formation of crescent-like nucleolar caps. Instead, UBTF-positive FCs gradually enlarged and decreased in number while remaining intranucleolar and tightly integrated within the ICC–PCC framework. Most likely, rDNA folded into structure of FC retained (at least partially) their basic molecular/structural properties even after severe ionizing radiation damage. Indeed, UBTF-positive fluorescence

was detected throughout the entire post-irradiation period, remaining bright and spherical even being redistributed among micronuclei. Moreover, 3D reconstructions demonstrated persistent ICC–PCC continuity and firm embedding of UBTF-positive FCs within NAC, even in severely damaged nuclei.

These observations define a non-classical, pre-segregated nucleolar state induced by physical genotoxic stress. Unlike chemical inhibitors, γ-irradiation does not disassemble FC-NAC architecture into caps but instead promotes progressive chromatin compaction and structural reorganization within an intact NAC scaffold. This distinction suggests that nucleolar responses to chemical and physical DNA damage are not uniform but depend critically on the nature of the stressor and the primary molecular targets involved. Hence, despite extensive damage, 3D analysis of UBTF-positive structures demonstrated remained integrated within NAC. Moreover, prolonged exposure to 30 Gy γ-irradiation was characterized by the emergence of giant, peripherally located UBTF-positive spheroids, never leading to formation of classical nucleolar caps, indicating profound stress-dependent reorganization of rDNA-associated domains.

4.3. Heat-Shock Elicits NAC-Centered Remodeling Distinct from Both Chemical and Radiation Stress

Heat-shock treatment induced yet another distinct pattern of reversible nuclear and nucleolar remodeling. Live-cell 2D/4D imaging combined with 3D analysis of UBTF-labeled cells revealed early and pronounced NAC alterations, particularly asymmetric coarsening and clumping leading to particular disorganization of the PCC shell. Nuclear contours relatively rapidly became irregular during heat 2.5 h exposure and continued to undergo folding and lobulation during recovery, occasionally progressing to amitotic fragmentation.

Similar to chemical nucleolar stress, heat-shock provoked pronounced apoptosis; however, unlike γ-irradiation, it did not induce extensive multinucleation in the majority of cells. Apoptotic degeneration developed asynchronously, with a substantial fraction of cells surviving and largely restoring smooth nuclear contours and intranucleolar clustering of UBTF-positive FCs by the end of the 24 h recovery period. Importantly, throughout all stages of heat-shock response and recovery, neither nucleolar cap formation nor asymmetrical enlargement of UBTF-positive FCs to giant spheroids was observed. Instead, UBTF-positive FCs exhibited relatively symmetric enlargement while remaining roundish and more loosely distributed throughout the nucleolar volume. Despite this spatial redistribution, UBTF-positive FCs remained structurally integrated within the NAC framework, indicating preservation of FC–NAC unity despite heat-shock–induced nucleolar stress and its associated apoptogenic remodeling. Thus, heat-shock, like γ-irradiation, induces a non-classical nucleolar response characterized by NAC reorganization without canonical pattern of nucleolar segregation. However, the less modified nuclear morphology and reversibility of accompanying structural disorders distinguish heat-shock from the irreversible, MC-dominated trajectory observed after γ-irradiation.

4.4. NAC as a Central Structural Determinant of Stress-Specific Nucleolar Responses

Taken together, our results identify NAC as a key structural and organizational determinant governing nucleolar responses to diverse stressors. Chemical inhibition of rRNA synthesis changes the behavior of FC–NAC couple, leading to nucleolar segregation obligatory leading to apoptotic commitment. In contrast, physical stressors such as γ-irradiation and heat-shock preserve FC-NAC integration, arresting nucleolar remodeling on pre-segregated nucleolar states associated with MC, delayed apoptosis, or recovery.

In this context, it is particularly noteworthy that chemical stress–induced classical nucleolar segregation, accompanied by formation of peripheral caps, coincides with extreme contraction of the NAC system. Specifically, by chemically-induced nucleolar stress the ICC network undergoes marked coarsening and collapse, followed by its complete fusion with the PCC shell [7, 8]. This large-scale NAC contraction appears to generate directional mechanical forces that displace the FCs toward the nucleolar periphery. As a result, GFP fluorescence corresponding to ICC becomes undetectable within the densely compacted residual nucleolus, which consists predominantly of GC.

These observations strongly suggest that canonical nucleolar cap formation is not merely a passive consequence of rRNA transcriptional inhibition, but a structurally driven process requiring coordinated ICC disassembly and its integration into the PCC shell. In other words, cap formation represents the terminal morphological outcome of NAC collapse. Accordingly, the absence of classical nucleolar caps following physical stressors likely reflects incomplete or qualitatively distinct NAC contraction, preserving ICC–FC structural continuity even in severely damaged cells.

Our specific interest in PCC is grounded in earlier studies describing the Perinucleolar Compartment (PNC) as a distinct molecular domain organized as tightly apposed chromatin blocks adjacent to the nucleolus [37–40]. Due to their topographic proximity, structural continuity, and functional association with RNA polymerase III transcription, PCC and PNC represent non-ribosomal chromatin domains that warrant particular attention. Their distinct responses to chemical and physical stressors—especially the stress-specific behavior of PCC following γ-irradiation and heat-shock — suggest differential regulatory mechanisms within the broader NAC system. The coordinated structural and functional interplay between non-ribosomal chromatin domains (PCC/PNC and ICC) and rDNA-containing chromatin within FCs remains insufficiently understood. Elucidating how these intra- and perinucleolar chromatin components interact under stress conditions will require integrated molecular and functional approaches. At present, the collective role of these chromatin–nucleolar interfaces in determining nucleolar stability, transcriptional regulation, and cell fate remains largely unexplored.

4.5. NAC-Centered Mechanistic Model of Stress-Specific Nucleolar Remodeling

Our findings support a unified structural hypothesis in which the NAC system — comprising PCC and ICC - acts as a mechanically and functionally integrated scaffold that governs nucleolar remodeling under stress. Within this framework, stress-induced nucleolar

reorganization is determined not simply by inhibition of rRNA transcription, but by the extent and mode of NAC contraction.

As it was noted, under chemical stress (e.g., AMD and Cis-Pt), classical nucleolar segregation coincides with extreme contraction and collapse of the NAC system, while condensation degree of PCC increased (thickening of PCC) and ICC network undergoes complete fusion with the PCC shell. This coordinated contraction of ICC and PCC likely generates directional structural forces that physically displace the FCs toward the nucleolar periphery. As a consequence, FCs coalesce into crescent-like caps positioned at the PCC – residual nucleolus interface. At this stage, GFP-positive ICC fluorescence becomes undetectable within the residual nucleolus, which consists predominantly of GC (7, 8). Thus, canonical cap formation represents the terminal morphological manifestation of global NAC collapse.

In contrast, physical stressors such as γ-irradiation and heat-shock do not induce complete NAC collapse. Although ICC compaction and PCC thickening occur, ICC-FC continuity is preserved. Even in severely damaged cells, enlarged UBTF-positive FCs remain structurally integrated within the NAC framework and retain intranucleolar localization. The absence of peripheral cap formation therefore reflects incomplete or qualitatively distinct NAC contraction. Rather than directional collapse, the NAC undergoes stress-specific remodeling that preserves FC–NAC unity.

This distinction is critical. In the chemical stress paradigm, nucleolar segregation appears to be driven by coordinated ICC disassembly and mechanical incorporation into the PCC shell, culminating in irreversible structural inactivation and rapid apoptotic progression. In the physical stress paradigm, NAC integrity is partially maintained, permitting prolonged remodeling, delayed cell fate decisions, and in some cases structural recovery.

Accordingly, we propose that the degree and topology of NAC contraction represent a structural checkpoint controlling nucleolar fate. Complete NAC collapse leads to canonical segregation, whereas partial NAC remodeling preserves intranucleolar organization despite profound cellular damage. In this view, the NAC is not a passive chromatin shell but a dynamic mechanical regulator of nucleolar architecture whose stress-specific behavior determines whether cells undergo rapid apoptosis, mitotic catastrophe, or structural recovery. This NAC-centered model integrates ICC dynamics, PCC behavior, FC enlargement, and cap formation into a single mechanistic framework and provides a structural basis for understanding why chemical and physical stressors generate fundamentally different nucleolar stress phenotypes.

4.6. Concluding Remarks

This study demonstrates that nuclear and nucleolar remodeling under stress follows distinct, stressor-specific trajectories that cannot be reduced to a single canonical pathway. By integrating long-term live-cell imaging with detailed 3D structural analysis, we show that γ-irradiation and heat shock induce non-classical, NAC-centered nucleolar remodeling fundamentally different from chemical stress–induced segregation. These findings highlight the importance of NAC architecture in maintenance of nucleolar integrity and shaping nucleolar stress responses. Hence, NAC can provide a structural framework for understanding how

different insults drive divergent cellular outcomes, including mitotic catastrophe, apoptosis, or recovery.

Acknowledgments

This work was financially supported by Administration Board and Academic Council of NVU. Authors express gratefulness to NVU directors and members of Academic Council for their efficient financial and technical engagement. Also, authors express thankfulness to Dr. V. Okuneva for cell cultivation, preparation of experimental samples, immunolabeling and other technical assistance.

REFERENCES

[1]. Mosgoller, W. (2003). Nucleolar Ultrastructure in Vertebrates. In The Nucleolus (ed Olson, M.O.) (Plenum Publisher, London), 1-11.
[2]. Boisvert, F. M., van Koningsbruggen, S., Navascués, J., & Lamond, A. I. (2007). The multifunctional nucleolus. Nat Rev Mol Cell Biol, 8, 574–585.
[3]. Hernandez-Verdun, D., Roussel, P., Thiry, M., Sirri, V., & Lafontaine, D. L. J. (2010). The nucleolus: structure/function relationship in RNA metabolism. Wiley Interdiscip Rev RNA, 1(3), 415–431.
[4]. Németh, A., Conesa, A., Santoyo-Lopez, J., Medina, I., Montaner, D., & Péterfia, B. (2010). Initial genomics of the human nucleolus. PLoS Genet, 6(3), e1000889.
[5]. van Koningsbruggen, S., Gierlinski, M., Schofield, P., Martin, D., Barton, G. J., & Ariyurek, Y. (2010). High-resolution whole-genome sequencing reveals that specific chromatin domains from most human chromosomes associate with nucleoli. Mol Biol, 21(21), 3735–3748.
[6]. Pederson, T. (2011) The nucleus introduced. Cold Spring Harb Perspect Biol, 3(5), a000521.
[7]. Tchelidze, P., Benassarou, A., Kaplan, H., O'Donohue, M-F., Lucas, L., Terryn, C., Rusishvili, L., Mosidze, G., Lalun, N., & Ploton, D. (2017). Nucleolar sub-compartments in motion during rRNA synthesis inhibition: Contraction of nucleolar condensed chromatin and gathering of fibrillar centers are concomitant. PLoS One, 12(11), e0187977.
[8]. Tchelidze, P., Kaplan, H., Terryn, C., Lalun, N., Ploton, D., & Thiry, M. (2019). Electron tomography reveals changes in spatial distribution of UBTF1 and UBTF2 isoforms within nucleolar components during rRNA synthesis inhibition. J Struct Biol, 208(2), 191–204.
[9]. Baserga, S. J., DiMario, P. J., & Duncan, F. E. (2020). Emerging roles for nucleolus 2019. J Biol Chem, 295(16), 5535–5537.
[10]. Mayer, C., & Grummt, I. (2005). Cellular stress and nucleolar function. Cell Cycle, 4(8), 1036–1038.
[11]. Drygin, D., Rice, W. G., & Grummt, I. (2010). The RNA polymerase I transcription machinery: An emerging target for the treatment of cancer. Annu Rev Pharmacol, 50, 131-156.
[12]. Michel, J., Nolin, F., Wortham, L., Lalun, N., Tchelidze, P., Banchet, V., Terryn, C., & Ploton, D. (2019). Various Nucleolar Stress Inducers Result in Highly Distinct Changes in Water, Dry Mass and Elemental Content in Cancerous Cell Components: Investigation Using Nano-Analytical Approach. Nanotheranostics, 3(2), 179–195.
[13]. Lafita-Navarro, M. C., & Conacci-Sorrell, M. (2022). Nucleolar stress: From development to cancer. Semin Cell Dev Biol, 136, 64–74.
[14]. Potapova, T. A., Unruh, J. R., Conkright-Fincham, J., Banks, C. A., Florens, L.,

Schneider, D. A., & Gerton, J. L. (2023). Distinct states of nucleolar stress induced by anticancer drugs. eLife, 12, RP88799.
[15]. Pigg, H. C., Alley, K. R., Griffin, C. R., Moon, C. H., Kraske, S. J., & DeRose, V. J. (2024). The unique Pt (II)-induced nucleolar stress response and its deviation from DNA damage response pathways. J Biol Chem, 300(11), 107858.

[16]. Yglesias, M. V., & DeRose, V. J. (2025). Nucleolar Stress-inducing Compounds Influence rDNA Occupancy of RNA Polymerase I Transcription Machinery. Preprint at bioRxiv DOI: https://doi.org/101101/2025.01.09.632225.
[17]. Imamura, R., & Yasuhara, T. (2025). Nucleolar Organization in Response to Transcriptional Stress. Cancer Sci, 116(10), 2649-2656.
[18]. Portugal, J., Mansilla, S., & Bataller, M. (2010). Mechanisms of drug-induced mitotic catastrophe in cancer cells. Curr Pharm Des, 16(1), 69–78.
[19]. Eriksson, D., & Stigbrand, T. (2010). Radiation-induced cell death mechanisms. Tumour Biol, 31(4), 363–372.
[20]. Kondo, T. (2013). Radiation-induced cell death and its mechanisms. Radiat Emerg Med, 2, 1–4.
[21]. Lee, C-H., Wu, S-B., Hong, C-H., Yu, H-S., & Wei, Y-H. (2013). Molecular Mechanisms of UV-Induced Apoptosis and Its Effects on Skin Residential Cells, The Implication in UV-Based Phototherapy. Int J Mol Sci, 14(3), 6414–6435.
[22]. Leskovac, A., Petrovic, S., Gus-Scekic, M., Vujic, D., & Joksic, J. (2014). Radiation-induced mitotic catastrophe in FANCD2 primary fibroblasts. Int J Radiat Biol, 90(5), 373–381.
[23]. Lombardi, D., & Lasagni, L. (2016). Cell-cycle Alterations in Post-Mitotic Cells and Cell Death by Mitotic Catastrophe. In Cell Cycle (ed Morata, G.) (InTechOpen, Rijeka). DOI: 10.5772/61783.
[24]. Roninson, I. B. (2017). Mitotic Catastrophe. In Encyclopedia of Cancer (ed Schwab, M.) (Springer, Berlin, Heidelberg). 2345–2347.
[25]. De Souza, R., Ayub, L. C., & Yip, K. (2017). Mitotic Catastrophe. In Apoptosis and Beyond: The Many Ways Cells Die (ed Radosevich, J.) (Wiley-Blackwell, Hoboken, NJ). Ch. 23, 475–510.
[26]. Azzouz, D., Khan, M. A., Sweezey, N., & Palaniyar, N. (2018). Two-in-one: UV radiation simultaneously induces apoptosis and NETosis. Cell Death Discov, 4, 51.
[27]. Mascaraque, M., Delgado-Wicke, P., Damian, A., Lucena, S. R., Carrasco, E., & Juarranz, A. (2019). Mitotic Catastrophe Induced in HeLa Tumor Cells by Photodynamic Therapy with Methyl-aminolevulinate. Int J Mol Sci, 20(5), 1229.
[28]. Adjemian, S., Oltean, T., Martens, S., Wiernicki, B., Goossens, V., Vanden Berghe, T., Cappe, B., Ladik, M., Riquet, F. B., Heyndricks, L., Bridelance, J., Vuylsteke, M., Vandecasteele, K., & Vandenabeele, P. (2020). Ionizing radiation results in a mixture of cellular outcomes including mitotic catastrophe, senescence, methuosis, and iron-dependent cell death. Cell Death Dis, 11(11), 1003.
[29]. Zhang, Z., Yang, J., Maimaitiyimin, R., Ma, M., Zhang, H., & Wang, R. (2020). Radiation-induced mitotic catastrophe is associated with down-regulated ribosomal biosynthesis and mitosis genes. All Life, 13(1), 474–485.
[30]. Reimann, H., Stopper, H., & Hintzsche, H. (2020). Long-term fate of etoposide-induced micronuclei and micronucleated cells in HeLa-H2B-GFP cells. Arch Toxicol, 94(10), 3553–3561.
[31]. Korsholm, L. M., Gál, Z., Bernáldez, B. N., Quevedo, O., Boukoura, S., Lund, C. C., & Larsen, D. H. (2020). Recent advances in the nucleolar responses to DNA double-strand breaks. Nucleic Acids Res, 48(17), 9449–9461.
[32]. Jiao, Y., Cao, F., & Liu, H. (2022). Radiation-induced Cell Death and Its Mechanisms. Health Phys, 123(5), 376–386.

[33]. Mikhalkevich, N., Russ, E., & Iordanskiy, S. (2023). Cellular RNA and DNA sensing pathways are essential for the dose-dependent response of human monocytes to ionizing radiation. Front Immunol, 14, 1235936.
[34]. Shav-Tal, Y., Blechman, J., Darzacq, X., Montagna, C., Dye, B. T., & Patton, J. G. (2005). Dynamic Sorting of Nuclear Components into Distinct Nucleolar Caps During Transcriptional Inhibition. Mol Biol Cell, 16(5), 2395–2413.
[35]. Nadaraia, L., Okuneva, V., Gogebashvili, M., Ivanishvili, N., & Tchelidze, P. (2024). Nucleolar Dynamics: Rearrangement of Nucleolus Associated Condensed Chromatin Under DNA Damage Induced by Different Doses of γ-irradiation. J Radiobiol Radiat Saf, 4(5), 18–36.
[36]. Nadaraia, L., Okuneva, V., Nanikashvili, M., & Tchelidze, P. (2025). 3D Visualization of Nuclear Damages in Histone H2B-GFP Tagged He-La Cells: Post-Irradiation Imaging. J Radiobiol Radiat Saf, 5(6), 55-70.
[37]. Slusarzyk, A., & Huang, S. (2008). The Perinucleolar Compartment (PNC): Detection by Immunocytochemistry. MIMB, 463, 161-167.
[38]. Pollock, K., & Huamg, S. (2010). The Perinucleolar Compartment. Cold Spring Harb Perspect Biol, 2(2), a0000679.
[39]. Pollock, C., Daily, K., Nguyen, V. T., Wang, C., Lewandowska, M. A., Bensaude, O. & Huang, S. (2011). Characterization of MRP RNA-protein interactions within the perinucleolar compartment. Mol Biol Cell, 22(6), 858-867.
[40] Makeyev, E., & Huang, S. (2024). The Perinucleolar Compartment: Structure, Function, and Utility in Anti-Cancer Drug Development. Nucleus, 15(1), 2306777.